Investigation of Monovalent Li and Divalent Ni Doping in Co_3O_4 for Enhanced Hydroelectric Cell Performance

Rajiv Kashyap [a, b], Aman Chauhan [c], Gurpreet Kaur [c], Ganga Ram Chaudhary [c] Martin J. Taylor [b*], Ramesh K Sharma [d*]

[a] Department of Physics, Panjab University, Chandigarh, 160014, India
[b] School of Engineering, Chemical Engineering, University of Hull, Hull, United Kingdom,
[c] Department of Chemistry, Panjab University, Chandigarh, 160014, India
[d] CIL/SAIF/UCIM, Panjab University, Chandigarh, 160014, India

Corresponding authors: ramesh@pu.ac.in, Martin.Taylor@hull.ac.uk

Abstract: The hydroelectric cell (HEC) produces green power at room temperature using non-photocatalytic water splitting. To achieve this goal, pure Ni (Nickel) and lithium (Li) substituted in cobalt oxide (Co_3O_4), a mesoporous oxygen-deficient material, is introduced. The substance splits water into H_3O^+ /OH^- ions by an electrolytic chain reaction, resulting in a 1.06 V potential difference between the electrodes. LCO-based HEC produced 39 mW of peak output (P_{out}) at 1.06 V. EPR spectroscopy and EIS curve have confirmed the presence of oxygen defects and ionic diffusion in Li-doped cobalt oxide materials. Similar to solar cells, an LCO-based HEC offers a low-cost, water-based method of producing green energy with the extra benefit of being able to function in the dark. The process also produces hydrogen gas (green hydrogen technology), which creates prospects for the manufacture of hydrogen, diversifying hydrogen supply chain options and developing new routes for industrial decarbonization, globally.

Keywords: cobalt oxide, oxygen vacancy, hydroelectric cell, solid-state sintering. renewable energy

Highlights:

1) Li and Ni substituted cobalt oxide was prepared via a solid-state synthesis route
2) 35 mW of power was obtained by Li doping which is 4 times higher than undoped cobalt oxide.
3) EPR spectra clear Li substitution increases the surface defects in the cobalt oxide.
4) Li substitution increases the specific surface area of the cobalt oxide by 8 times.

1.0 Introduction

Due to the exponential growth in global energy consumption brought about by the expansion of industrial production and the growing global population, there is a significant reliance on fossil fuels such as coal, oil, and natural gas [1,2]. Unfortunately, the environment and public health are harmed by the excessive CO_2 emissions that have resulted from this reliance on conventional energy sources [3]. To address these problems and meet the growing need for energy, researchers are actively searching for sustainable, environmentally friendly, and low-carbon alternative energy sources [4,5]. The solution to the energy problem and ensuring a stable economy and energy supply for the future lies in the development and utilization of non-traditional energy sources [6].

However, their contribution to the world's energy output is still very small due to several operational and implementation challenges [7]. For example, photovoltaic technology has demonstrated potential. Still, the high installation costs, short solar beam duration, and locational and climate restrictions limit large-scale energy production [8,9]. In the same way, the airflow requirements for wind turbines and ocean energy systems restrict their general application [10]. Among other issues, worries about safety and high costs have hindered the widespread adoption of fuel cells and hydrogen. As a result, innovators are striving to develop improved renewable energy sources that can be used to overcome these limitations and make serious headway in global decarbonization efforts [11,12]. In the past ten years, mesoporous oxide materials have gained interest due to their advantageous properties, which include their large specific surface area, tunable porous structure, and remarkable stability [13,14]. Numerous industries have exploited these materials, including energy conversion and storage, sensors, and catalysis [15].

This work focuses on using cobalt oxide in the presence of nickel and lithium entities to improve hydroelectric cell applications' efficiency. Due to its exceptional magnetic and electrical properties, as well as exhibiting p-type semiconducting behavior, cobalt oxide is a low-cost candidate for energy production [16,17]. Hydroelectric current is produced as a result of the persistent dissociation of water molecules brought on by this process, which also creates a strong electric field [18,19]. Compared to traditional electrochemical cells, which depend on electrolytes, hydroelectric cells provide several advantages, including being sustainable, simple to manufacture, lower cost than, alternative, and does not require electrolytes. Previous studies have looked at the hydroelectric cells' unloaded power output that is successfully made from different metal oxides. In this investigation, we investigate the effects of monovalent Li^+ and bivalent Ni^{2+} doping on the structural and morphological characteristics of Co_3O_4, as well as the efficiency of this material as a hydroelectric cell material. The water dissociation process can be accelerated by creating oxygen defects through ion doping, changing the characteristics of cobalt oxide-based hydroelectric cells.

The doped Co_3O_4 samples are made using the affordable and scalable synthesis method known as solid-state sintering. Co_3O_4 produced 9mW of power by 5 μL of water whereas Ni doping in Co_3O_4 increases the efficiency to 2.5 times and Li doping increases the efficiency to 4 times. The hydroelectric cell's performance as a voltage source, its ability to generate power, and its efficiency will all be carefully tested and examined with changing loads. The results of this study could be extremely helpful in designing and perfecting new materials for effective and environmentally friendly energy conversion.

2.0 Material and Methods

2.1 Chemicals

Analytical grade cobalt (II) carbonate ($CoCO_3.xH_2O$, 99.5%), lithium carbonate ($Li(CO_3)_2.6H_2O$, 98%) and nickel carbonate ($NiCO_3.2Ni(OH)_2.4H_2O$, 99.5%) were acquired from Thermo Scientific Chemicals. Silver paste of 99.9% and zinc sheet of 98% purity were acquired from Thermo Scientific and used without further processing.

2.2 Synthesis of Co_3O_4 and Li and Ni -substituted Co_3O_4-

Lithium carbonate ($Li(CO_3)_2.6H_2O$), cobalt carbonate ($CoCO_3.xH_2O$), and nickel carbonate ($NiCO_3.2Ni(OH)_2.4H_2O$) salts were weighed following their stoichiometric ratios to synthesize 10 wt % Li-substituted Co_3O_4 and 10 wt % Ni-substituted Co_3O_4. The precursors were uniformly mixed for 1 h in a pestle and mortar with acetone (20mL) (Fisher Scientific, Analytical Grade), and the dried material was then calcined at 800°C in a muffle furnace for 5 H ramping at 5 degrees per minute. The resulting powder was then pelletized into 3.5 cm circular pellets of thickness ~1 mm and heated for 2 h in an oven at 900°C. These pellets designated LCO and NCO respectively for 10% lithium and 10% nickel doping, served as the materials for hydroelectric cells (HECs). The pellet had silver paste designed as a cathode on one side and a zinc layer that functioned as the anode. The wires were attached to the electrodes with the help of soldering and hence the circuit was completed.

2.3 Testing of HEC

The method begins with testing the constructed HEC with a few water droplets, followed by applying reverse polarity current to get a voltage measurement of zero. The open circuit current (Ioc) corresponds to zero voltage, whereas the greatest voltage obtained is the open circuit voltage (Voc). The three-electrode configuration is then converted into a two-electrode system by connecting the counter and reference electrodes for impedance analysis. Impedance spectroscopy is then used to assess the electrical characteristics of the HEC in both dry (before water application) and wet circumstances (post-water application).

3.0 Characterization

To validate the crystalline structure of the sample, Malvern Panalytical X'Pert Pro X-ray diffractometer (XRD) was used to acquire diffractograms using Cu-Kα radiation with a wavelength of 1.54 Å. The diffraction angles monitored were from 20°-80° during the investigation, with 0.02° increments between each step. For Fourier-transform infrared (FT-IR) measurements, a Perkin Elmer Spectrum 400 spectrometer was used in the range of 400–4000 cm^{-1} where a 1μm thick pellet is made with KBr. Morphological analysis was carried out using a Hitachi SU8010 Field-Emission Scanning Electron Microscope (FESEM). The V-I (voltage-current) characteristics of several hydroelectric cells were graphed using a Keithley-2602 source meter. To determine the ionic conduction and impedance of the material synthesized, Nyquist plots were recorded using a Metrohm Electrochemical workstation where Ag/AgCl (Silver chloride) and a platinum plate served as the reference and counter electrodes, respectively to plot the impedance curve in the frequency range of 20 Hz–120 MHz.

4.0 Results and Discussion

4.1 XRD

As seen in the X-ray spectral diffractograms in **Figure 1** (a-d)), crystalline Co_3O_4, Li substituted Co_3O_4 and Ni substituted Co_3O_4 calcined at 900 ºC give reflection peaks centered at $2\theta \approx 31.35°$, 44.88°, 49.31°, 59.46° and 65.30°, that correspond to the (220), (311), (400), (511), (440) crystal planes for Co_3O_4 [20]. For LCO and NCO, all of the observed diffraction peaks were the same as those of the pure Co_3O_4. There is a slight shift towards higher 2θ for the most intense peak (311), after Li and Ni substitution.

Equation 1 is the Debye-Scherrer formula that has been utilized to estimate the crystallite size of Co_3O_4 in all three materials investigated. This information is presented in **Table 1.** It was found that after the substitution of Ni and Li the overall Co_3O_4 crystallite size decreased from 40.45 > 37.90 > 36.36, respectively. **Table 1** also demonstrates indisputably the strain (ε) and dislocation density (δ) calculated by **Equation 2** and **Equation 3** in the Co_3O_4 sample. Microstrain was found to rise after substitution, this indicates that the metal addition is not simply deposited on the surface of the Co_3O_4 but incorporated into the oxide matrix, potentially present in oxygen vacancies generated during calcination.

$$D = \mathrm{k}\lambda / \ \beta_{\mathrm{hkl}}\cos\theta \qquad \text{Equation 1}$$

$$\varepsilon = \frac{\beta cos\theta}{4} \qquad \text{Equation 2}$$

$$\delta = {}^{1}/_{D^2} \qquad \text{Equation 3}$$

Table 1. Crystallite size, micro-strain, and dislocation density of Co_3O_4 and **Li and Ni-doped Co_3O_4 samples.**

Sample	Angle (2θ)	FWHM (β)	Crystallite size (D) (nm)	Micro-strain (ε)	Dislocation density (δ) (nm^{-2})
Co_3O_4	36.89	0.207	40.45	0.0144	69.01
Ni-Co_3O_4	37.02	0.221	37.90	0.0158	63.02
Li-Co_3O_4	36.92	0.230	36.36	0.0162	61.64

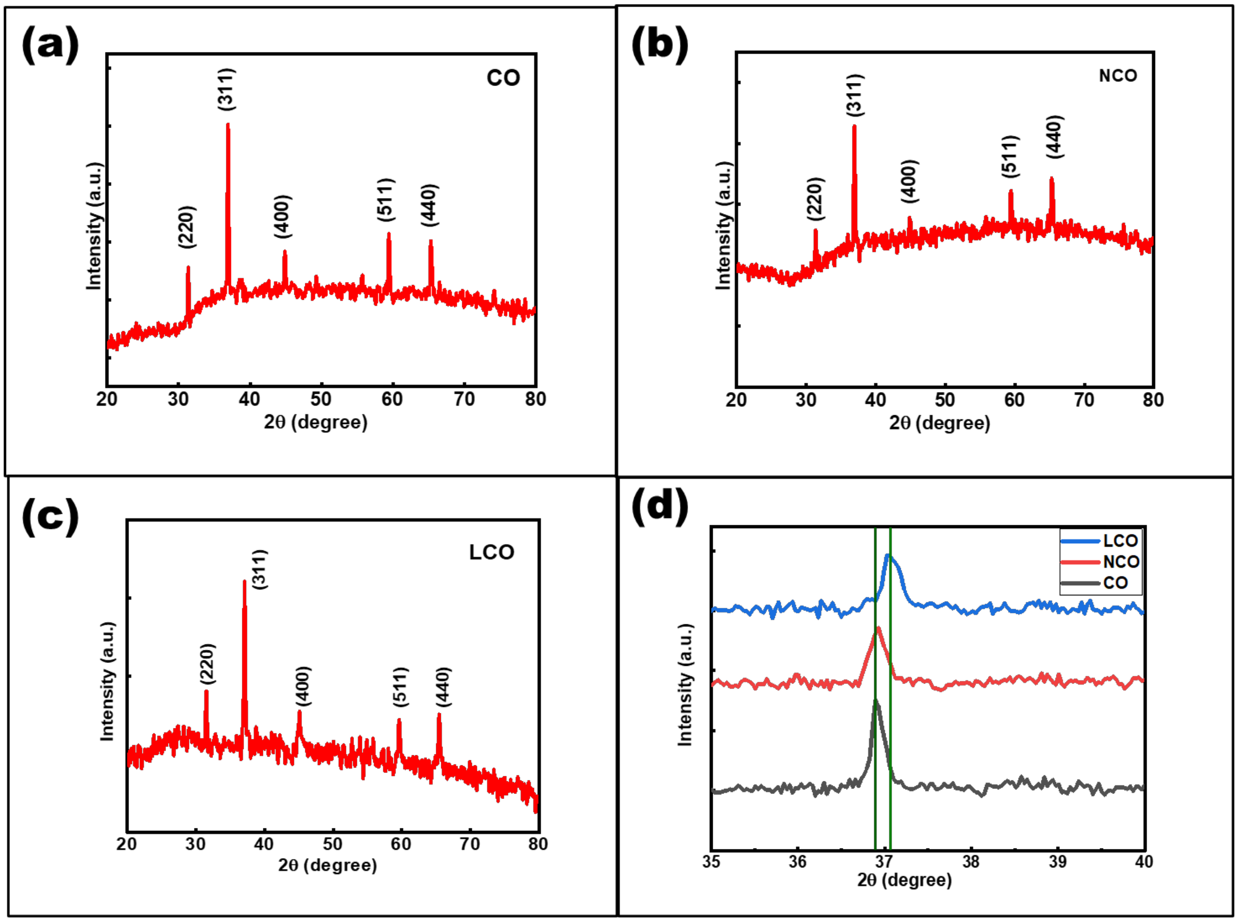

Figure 1 XRD pattern of a) cobalt oxide, b) Ni doped cobalt oxide, c) Li doped cobalt oxide, and d) peak shift in (311) peaks after doping.

4.2 FESEM

The surface morphology of Li and Ni-substituted cobalt oxide was examined using images of FESEM micrographs of LCO and NCO samples. The produced sample's distinctive crystallite shape is seen in the micrographs, structurally the shape doesn't deform or substantially alter but the overall grain size was found to reduce, post-metal introduction. The grain sizes measured were in the range of 70 - 100 nm for CO, LCO, and NCO, respectively. These measurements were found to agree with the estimated crystallite size from the X-ray diffraction. The changes in intergranular porosity are shown in **Figure 2(a-f)**, across two magnifications per sample.

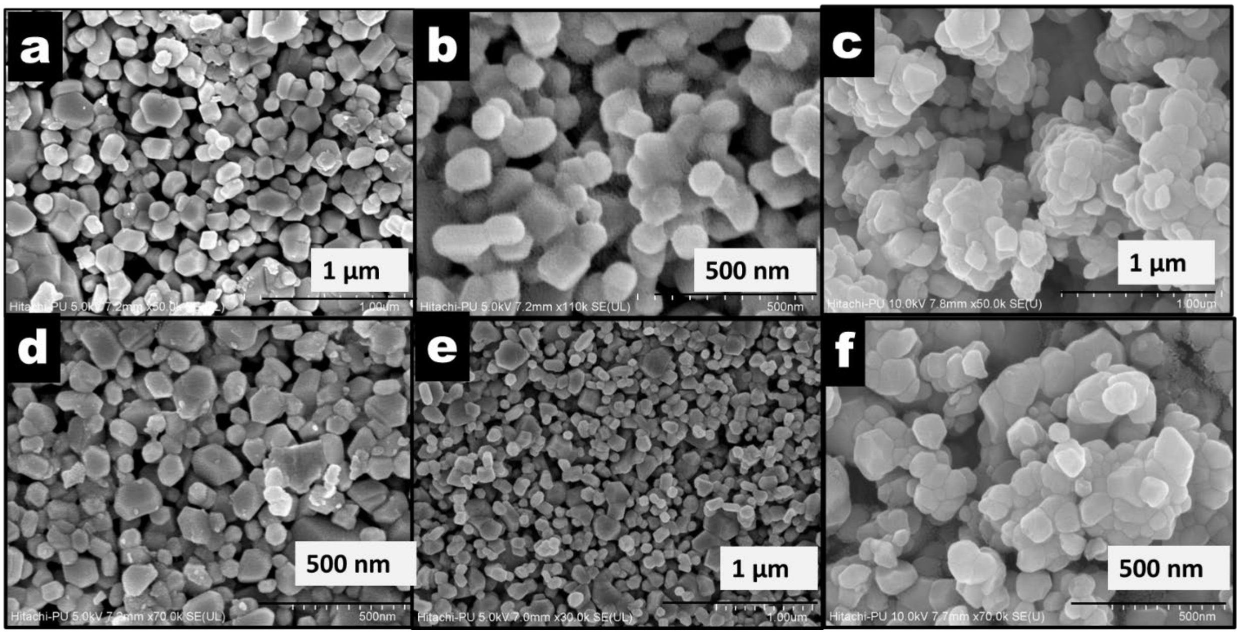

Figure 2 FESEM images of (a, b) CO, (c, d) NCO, (e, f) LCO

4.3 FTIR

Figure 3a displays the FTIR spectra for CO, LCO, and NCO samples across 400–4000 cm^{-1}, allowing the identification of a range of possible vibrational modes. Moisture in the samples, both adsorbed and atmospheric is the cause of a large absorption band around 3446 cm^{-1} that is attributed to the broad O–H stretch [21]. The peak at 1613 cm^{-1} corresponds to a second OH^{-} stretching vibration. These peaks broaden with Ni and Li doping, the highest intensity peak was observed for the LCO, demonstrating the increased capacity of the LCO sample to adsorb additional water via hydrogen bonding creation, as well as indicating potential hygroscopic behavior. Peaks at 663 cm^{-1} (v_1) are due to the vibration bond Co (III)-O and 576 cm^{-1} (v_2) are due to the stretching Co-O bond, which confirms the production of cobalt oxide material, which is another noteworthy characteristic [22].

4.4 EPR

Unpaired electrons are found on the surface of materials using electron paramagnetic resonance (EPR) techniques, which can reveal information about the presence of surface defects in the material. **Figure 3b** shows the EPR results obtained from CO, NCO, and LCO materials. Using the above **equation 4**, the constant g was calculated where the remaining terms are as follows: Planck's constant (h), microwave frequency (f), Bohr magneton (B), and magnetic field (H).

$$g = {}^{hf}/_{\mu_B H}$$ Equation 4

For all three samples (CO, NCO, LCO), EPR spectra show an oxygen vacancy signal with a g-factor of 2.003, 2.003, and 2.005, respectively. According to the spectra, all samples had the same major defect centers, as well as a few smaller minor paramagnetic centers. It is clear from a closer look at the peak that the oxygen vacancy signal intensity rises from CO >NCO > LCO, displaying the highest peak intensity. This finding supports a rise in the number of oxygen vacancies on the surface of the material, induced by calcination of the parent Co_3O_4. There are various benefits to having oxygen vacancies in increasing the activity of material in boosting water splitting capability [23, 24, 25, 26, 27]. It expands the activation adsorption sites for oxygen molecules that have been activated, facilitating a more effective adsorption process. In turn, this improvement has been found to benefit water splitting in hydroelectric cells (HEC), improving efficiency. Overall, the EPR characterization results are consistent with the theory that when oxygen vacancies develop from CO to NCO and then to LCO, their concentrations/dispersion do as well. The activation and adsorption processes are enhanced by this change in oxygen vacancy concentration, which eventually improves water splitting and boosts the HEC's effectiveness.

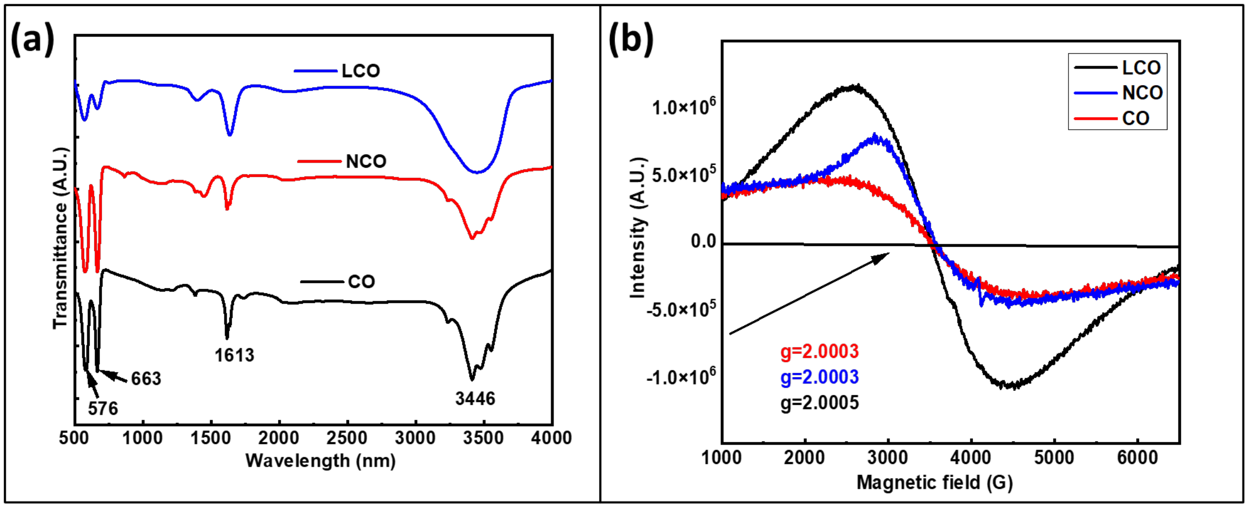

Figure 3 (a) FTIR Spectra and **(b)** Room-temperature EPR spectra of CO, NCO, and LCO respectively

4.5 Nitrogen physisorption (BET)

Nitrogen adsorption and desorption isotherms were used in BET measurements to gather knowledge of the specific surface area, pore diameter, and pore size distributions of the CO, NCO, and LCO samples. The nitrogen absorption-desorption isotherms for each sample are shown in Figure 4 (a, c, e) which shows Type IV curve behavior, leading to slight mesoporous characteristics [28]. Comparing the LCO sample to the CO and NCO samples, the LCO sample has the highest specific surface area of ~16.577 m^2/g, as shown in **Table 2**. This means that not only did the crystallites decrease in overall size (XRD and FESEM) as Ni and Li were introduced for each material, but the overall available surface area increased. From the bare CO, we witnessed an increase in surface area of 349% for NCO and 609% for LCO. Additionally, this increase in surface area also developed marginally larger pore diameters and corresponding pore volumes, for both metal-doped Co_3O_4 materials. One of the potential explanations for LCO's improved current output over the other hydroelectric cells (HECs) under consideration is that it has a larger specific surface area than CO and NCO as shown in **Table 2**.

Table 2 Surface parameters obtained by BJH analysis

Sample	Pore Diameter (nm)	Pore volume (cc/g)	Surface area (m^2/g)
CO	1.69	0.029	2.72
NCO	2.18	0.015	9.50
LCO	3.05	0.093	16.58

Rapid charge storage is made possible through the developed mesoporosity, which makes it easier for hydroxide ions to get the electrochemically active spots. The LCO sample's higher porosity and comparatively larger specific surface area result, in comparison to the base CO, provides a greater available contact area that facilitates the water-splitting mechanism and increases current generation.

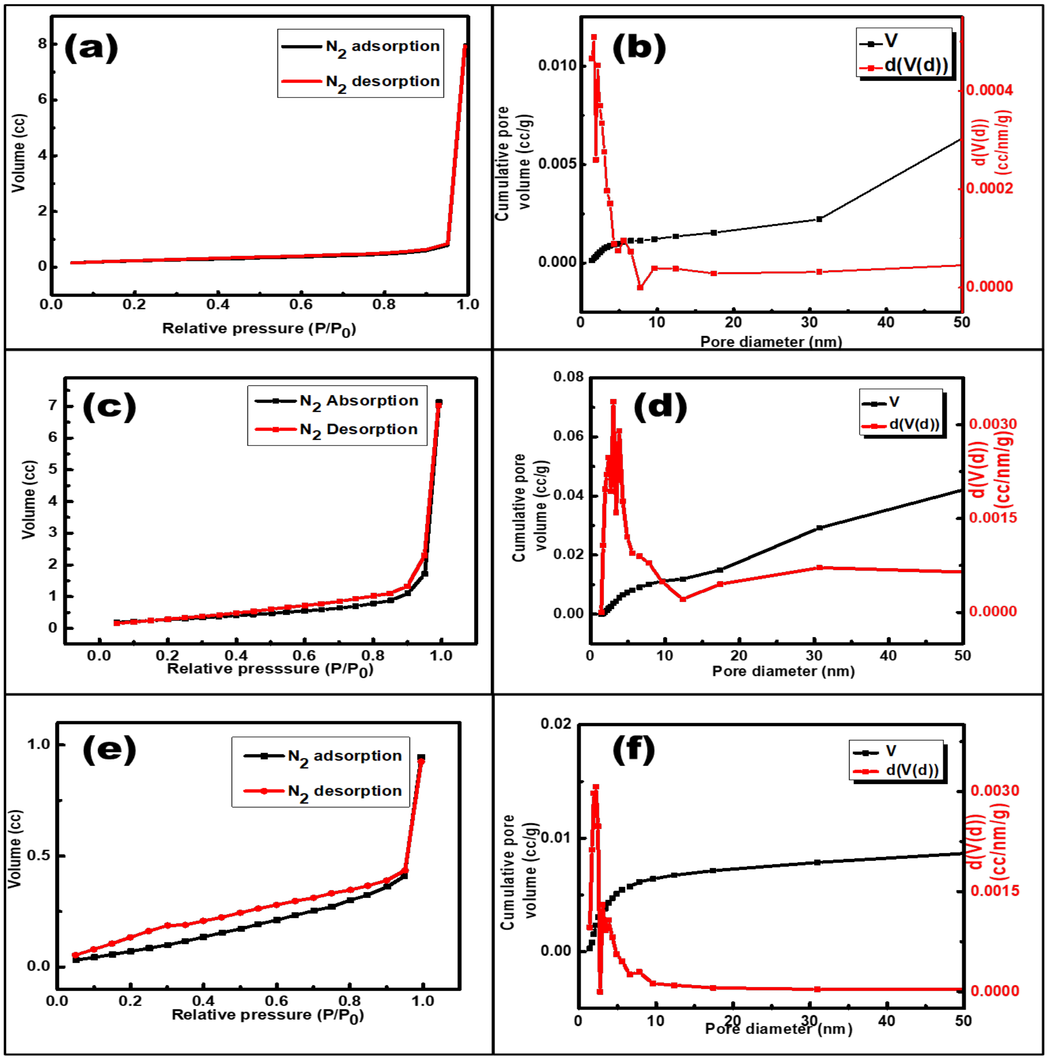

Figure 4 Nitrogen adsorption-desorption isotherm and pore size distribution of (a, b) CO, (c, d) NCO, and (e, f) LCO

4.6 HEC (Hydroelectric cell)

Surface cations that are not completely coordinated or saturated are known to exist in metal oxides. Cobalt oxide's oxygen vacancies and these surface cations combine to produce ideal conditions for water adsorption. As shown by X-ray diffraction, FT-IR, and EPR spectroscopy, the creation of defects within the parent material is caused by the differing oxidation numbers and ionic radii of lithium and nickel ions. When distilled water droplets come into contact with the oxide surface, their oxygen-deficient structure attracts and activates water molecules, causing them to dissociate into hydroxide (OH^-) and hydronium (H_3O^+) ions (**Figure 5**). Water molecules are made up of two elements: oxygen, which is electronegative, and hydrogen, which is electropositive. Hydroxide ions, on the other hand, are electron-rich and frequently transfer their electrons. Therefore, through hydrogen bonding, hydroxide ions aid in the dissociation of physically adsorbed water molecules, leading to the creation of additional hydroxide and hydronium ions. Some hydronium ions enter and physisorbed to the surface of the cobalt oxide, creating a strong electric field that causes water molecules to spontaneously dissociate. When the dissociated ions move in the direction of the corresponding electrodes (zinc and silver), these processes work together to produce an electric current. The reason behind the selection of the Zn electrode is the ejection of 2 electrons when it combines with OH- ions. Also, the Zn and Ag pair completes an anode-cathode pair to give a potential difference of 0.98V. The theoretical value of potential generated by the Zn and Ag electrode is 0.98 V as shown by **Equations 5, 6,** and **7**.

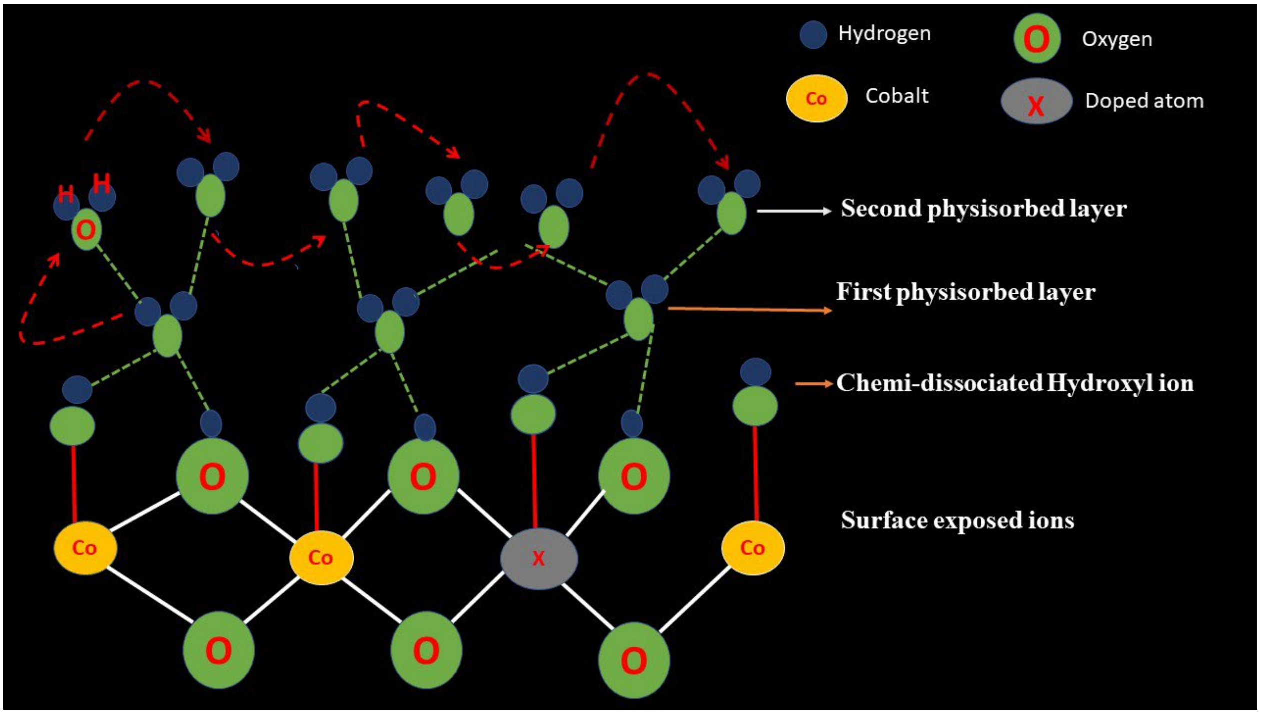

Figure 5 Water splitting and charge transfer mechanism on the surface of HEC through the Grothuss mechanism

At the Cobalt oxide surface:

$$H_2O \rightarrow H^+ + OH^- \qquad \textbf{Equation 5}$$

At Zn anode:

$$Zn + OH^- \rightarrow ZnOH_2 + 2e^- \ \ (-0.76 \text{ V}) \qquad \textbf{Equation 6}$$

At Ag cathode:

$2H^+ + 2e^- \rightarrow H_2$ (0.22) **Equation 7**

Total cell Electromagnetic field: 0.22 V − (−0.76 V) = 0.98 V

The affinity of OH^- ions is increased in the doped cobalt oxide due to the existence of polaronic defects, which makes it easier for them to migrate toward the zinc electrode through minor polaron hopping. With more Li and Ni doping, this results in strong ionic conductivity and a decrease in internal resistance. The Grotthuss process, on the other hand, drives H_3O^+ ions via the physically deposited water surface layer toward the silver electrode. A sustained electrical current is produced as a result of the continual dissociation of water molecules on the cobalt oxide surface, as a result of a redox reaction. A hydroelectric cell (HEC) is a type of cell that produces an electric current. Figure 5 illustrates the reactions that take place at the various electrodes.

4.8 Electrochemical Impedance Spectroscopy (EIS)

Nyquist plots produced from electrochemical impedance spectroscopy were used to investigate hydroelectric cells (HEC) under both dry and wet circumstances. In dry circumstances, the hydroelectric cell impedance, notably for Co_3O_4, Li-substituted Co_3O_4, and Ni-substituted Co_3O_4 samples, was very high, in the megaohms (MΩ) range. This increased impedance was corroborated by EPR studies, which attributed it to the mildly porous characteristic of the materials and the prevalence of flaws, as indicated by a varying g-factor. The dry HEC impedance profile displayed two unique features: a semicircle showing charge transfer and a straight line representing the ion diffusion process [29,30]. While the diameter of the semicircle in the high-frequency region indicates the resistance in charge transport between the electrode surface and the electrolyte, the linear component in the low-frequency zone frequently demonstrates diffusion-restricted processes. The addition of water to the HEC resulted in a significant reduction in impedance as shown in **Figure 6(a-c)**, implying the participation of charge moment processes and water molecule dissociation. Water is ionized by particular active sites such as Vo and surface defects in the material, resulting in chemo-dissociation. As a result, the cell's impedance decreased dramatically from MΩ to Ω (x10^6 decrease). Furthermore, LCO's wet state grain resistance was 5.1 Ω, compared to 11 Ω for NCO and CO samples, respectively.

The impedance values applied to grains and grain boundaries become extremely important in dry HECs when no ions move through the bulk. LCO has a lower charge transfer resistance than CO and NCO, implying better conductivity. The decreased diameter of the Nyquist plot provides more evidence. Ion diffusion into the electrode is responsible for the presence of a tail in the low-frequency zone.

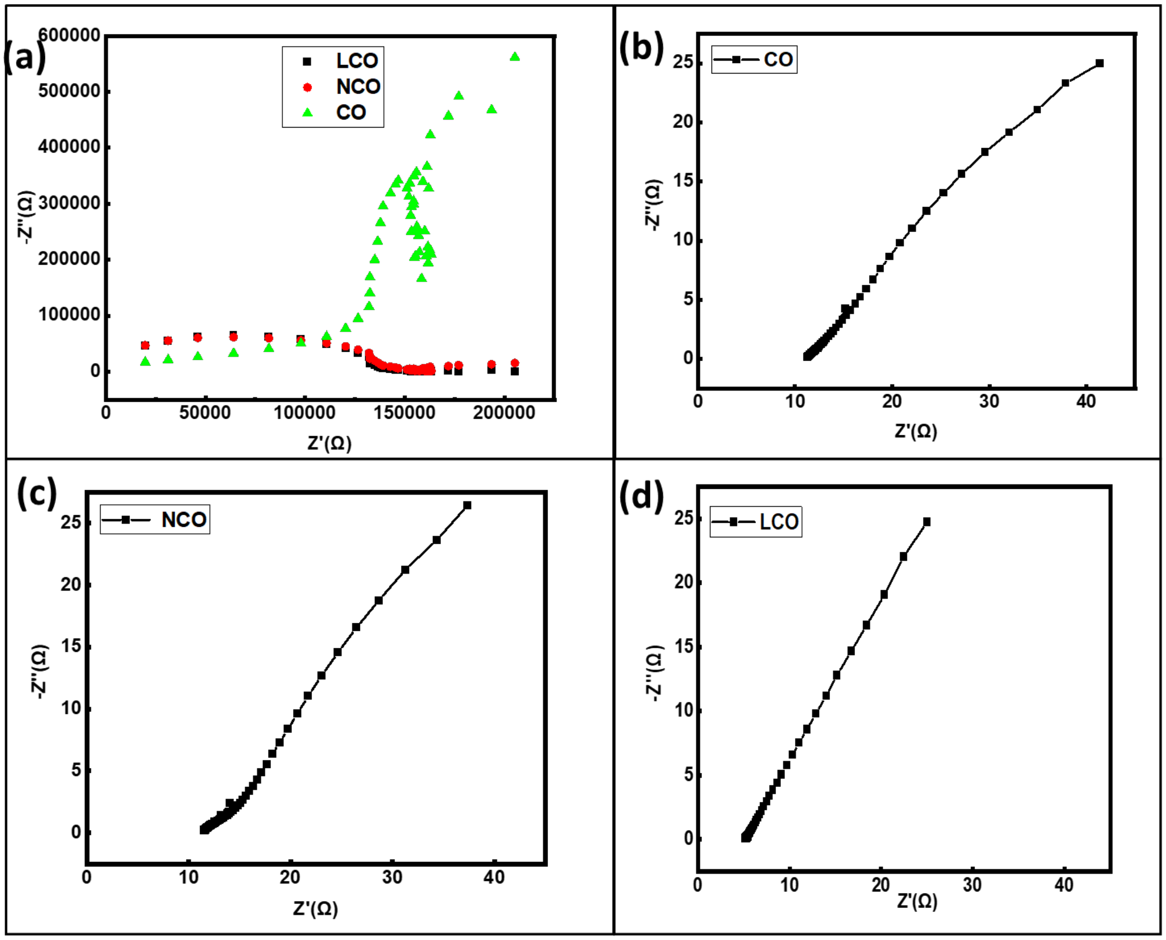

Figure 6 Room-temperature EIS spectra of a) dry CO, NCO, and LCO, b) Wet CO, (c) wet NCO, and (d) wet LCO

4.9 V–I characteristics of different cobalt oxide HEC

Figure 7 shows V-I polarization graphs of CO, NCO, and LCO cells, which exhibit a voltage decrease as the current approaches its maximum value. The Grotthuss chain reaction, on the other hand, counteracts this decrease, assisting in the current generation. The V-I polarization diagram distinguishes four loss regions: AB, BC, CD, and DE. The AB area corresponds to the largest voltage departure from the theoretical value (0.98 V), which is referred to as internal loss and is caused by grain discontinuity [31,32]. The activation loss area (BC) is the first barrier encountered by dissociated ions. The activation loss for CO, NCO, and LCO is 0.18 V, 0.16 V, and 0.03 V, respectively. This indicates that NCO requires less activation potential for a current start, most likely due to decreased resistance under wet circumstances, as validated by EPR.

Once the activation potential is overcome, the current flows freely, as shown by the CD part, which indicates the ohmic loss zone and shows a roughly linear connection. The internal ohmic resistance is caused by the high resistance of the oxide material, distilled water, and electrodes [33]. In terms of current, the DE area represents the saturation period. Voltage loss occurs as a result of mass concentration polarization or ion mass transport constraints, which limit ion mobility as current density increases. CO, NCO, and LCO cells outperform prior hydroelectric cells with maximum unloading currents of 12.2 mA, 29.7 mA, and 37.1 mA, respectively. The corresponding potentials are 0.80 V, 0.82 V and 0.95 V. Their respective maximum offload power capacities are 9.76 mW, 24.35 mW, and 35.24 mW. **Table 3** summarizes these cell properties, implying that they can light LEDs, fan bulbs, etc. by connecting a few cells in series and creating a few watts of electricity.

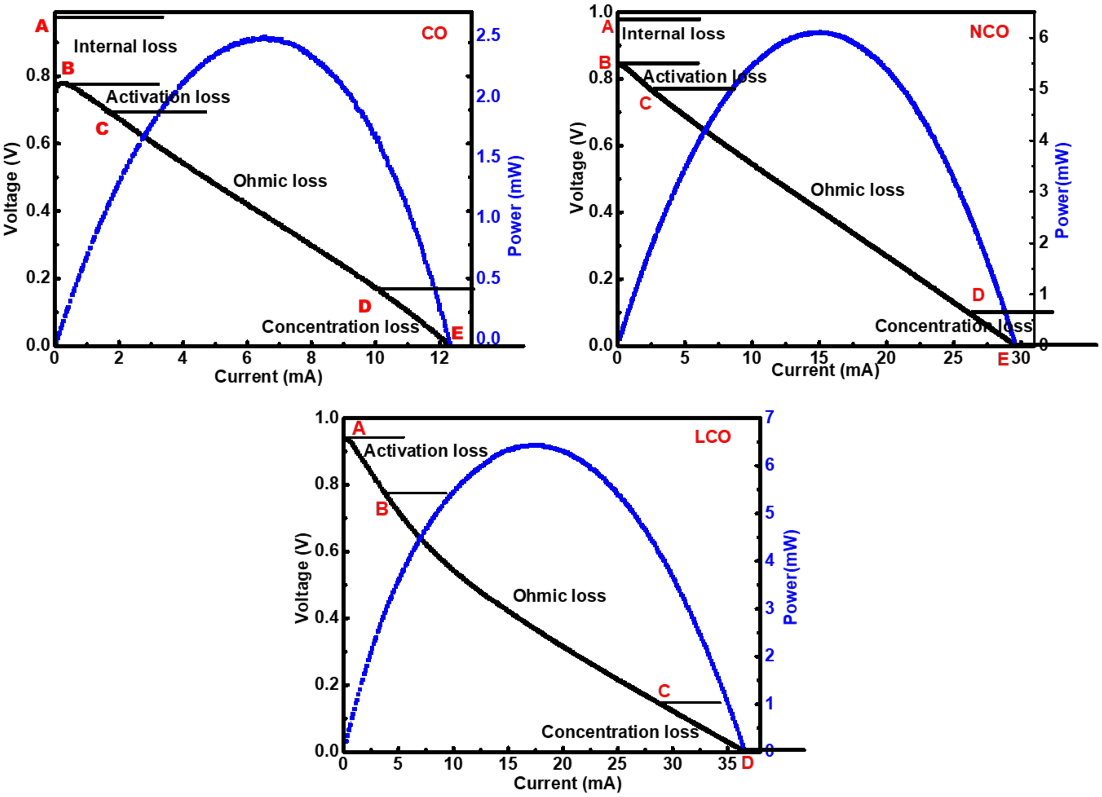

Figure 7 Voltage−current (V−I) polarization plots of (a) CO, (b) NCO and (c) LCO-based hydroelectric cell

Table 3; Voltage, Power, and current generation by an HEC

Sample	Voltage (V)	Current (mA)	Peak Power (mW)
CO	0.80	12.2	9.76
NCO	0.82	29.7	24.35
LCO	0.95	37.1	35.24

5.0 Conclusion

Mesoporous cobalt oxide (CO), nickel-doped cobalt oxide (NCO), and lithium-doped cobalt oxide (LCO) with oxygen deficiencies were produced using a simple solid-state reaction method. This was accomplished by depleting the oxygen content of the Co_3O_4 lattice and creating significant oxygen deficiency by adding metallic dopant lithium and transition metal dopant nickel. The surface of LCO was lithium-rich, resulting in a significant density of oxygen defect (Vo) centers as well as the highest specific surface area compared to the bare Co_3O_4 and Ni-doped Co_3O_4. These significant modifications allowed for excellent water molecule chemical dissociation, which was followed by physical dissociation, resulting in favorable ionic conduction inside the hydroelectric cell. A high density of short circuit current (Isc ~37 mA) and maximum power (P_{out} ~35 mW) were displayed by the LCO-based hydroelectric cell. This demonstrates the potential for replacing fuel cells and solar cells, albeit at this stage a small scale. However, it is postulated that this can be rapidly upscaled to be used for true decarbonization activities.

Credit authorship contribution statement

Rajiv Kashyap: Experimental work, Methodology, Data curation, Writing – original draft. **Aman Chauhan:** Methodology, Writing – review & editing. **Gurpreet Kaur.**: Data presentation, editing. **Ganga Ram Chaudhary**: Formal analysis, Supervision, Writing – review & editing. **Martin J Taylor:** Supervision, Writing – review & editing **Ramesh K Sharma**: Conceptualization, Resources, Writing – review & editing, Supervision.

Acknowledgements

RK, MJT and RKS acknowledge the Commonwealth split-site fellowship Programme (INCN-2023-169) for a split-site award. RK would also like to thank CSIR for the senior research fellowship with file number 09/135(0890)-2019-EMR-I.

References

---

[1] Amir, M., Deshmukh, R.G., Khalid, H.M., Said, Z., Raza, A., Muyeen, S.M., Nizami, A.S., Elavarasan, R.M., Saidur, R. and Sopian, K., 2023. Energy storage technologies: An integrated survey of developments, global economical/environmental effects, optimal scheduling model, and sustainable adaption policies. Journal of Energy Storage, 72, p.108694.

[2] Olabi, A.G., Onumaegbu, C., Wilberforce, T., Ramadan, M., Abdelkareem, M.A. and Al–Alami, A.H., 2021. Critical review of energy storage systems. Energy, 214, p.118987.

[3] Bertoncini-Silva, C., Zingg, J.M., Fassini, P.G. and Suen, V.M.M., 2023. Bioactive dietary components—Anti-obesity effects related to energy metabolism and inflammation. BioFactors, 49(2), pp.297-321.

---

[4] Chang, J., Leung, D.Y., Wu, C.Z. and Yuan, Z.H., 2003. A review on the energy production, consumption, and prospect of renewable energy in China. Renewable and Sustainable Energy Reviews, 7(5), pp.453-468.

[5] Kannan, N. and Vakeesan, D., 2016. Solar energy for future world:-A review. Renewable and sustainable energy reviews, 62, pp.1092-1105.

[6] Al-Shahri, O.A., Ismail, F.B., Hannan, M.A., Lipu, M.H., Al-Shetwi, A.Q., Begum, R.A., Al-Muhsen, N.F. and Soujeri, E., 2021. Solar photovoltaic energy optimization methods, challenges and issues: A comprehensive review. Journal of Cleaner Production, 284, p.125465.

[7] Isikgor, F.H., Zhumagali, S., T. Merino, L.V., De Bastiani, M., McCulloch, I. and De Wolf, S., 2023. Molecular engineering of contact interfaces for high-performance perovskite solar cells. Nature Reviews Materials, 8(2), pp.89-108.

[8] Brownson, D.A., Kampouris, D.K. and Banks, C.E., 2011. An overview of graphene in energy production and storage applications. Journal of Power Sources, 196(11), pp.4873-4885.

[9] Kumar, V., Pandey, A.S. and Sinha, S.K., 2016, March. Grid integration and power quality issues of wind and solar energy system: A review. In 2016 International conference on emerging trends in electrical electronics & sustainable energy systems (ICETEESES) (pp. 71-80). IEEE.

[10] Dai, K., Bergot, A., Liang, C., Xiang, W.N. and Huang, Z., 2015. Environmental issues associated with wind energy–A review. Renewable energy, 75, pp.911-921.

[11] Mittal, R., Sandhu, K.S. and Jain, D.K., 2010. An overview of some important issues related to wind energy conversion system (WECS). International Journal of Environmental science and development, 1(4), p.351.

[12] Hu, X., Zuo, D., Cheng, S., Chen, S., Liu, Y., Bao, W., Deng, S., Harris, S.J. and Wan, J., 2023. Ultrafast materials synthesis and manufacturing techniques for emerging energy and environmental applications. Chemical Society Reviews.

[13] Krusin-Elbaum, L. and Wittmer, M., 1988. Conducting transition metal oxides: possibilities for RuO2 in VLSI metallization. Journal of the Electrochemical Society, 135(10), p.2610.

[14] Neouze, M.A. and Schubert, U., 2008. Surface modification and functionalization of metal and metal oxide nanoparticles by organic ligands. Monatshefte für Chemie-Chemical Monthly, 139, pp.183-195.

[15] Danish, M.S.S., Bhattacharya, A., Stepanova, D., Mikhaylov, A., Grilli, M.L., Khosravy, M. and Senjyu, T., 2020. A systematic review of metal oxide applications for energy and environmental sustainability. Metals, 10(12), p.1604.

[16] Kashyap, R., Chauhan, M., Shah, J., Kotnala, R.K., Kaur, G. and Sharma, R.K., 2023. A novel device to generate green electric energy by water splitting at room temperature: Enhancing the efficacy by tuning nickel oxide thru lithium substitution. Materials Today Communications, 35, p.105661.

[17] Saini, A., Kashyap, R., Rani, J. and Sharma, R.K., 2023. Electrical energy of the order of 24 W/m^2 from water splitting using nickel oxide: Effect of synthesis process on power output. Results in Chemistry, 5, p.100911.

[18] Wang, S., Chen, P., Bai, Y., Yun, J.H., Liu, G. and Wang, L., 2018. New $BiVO_4$ dual photoanodes with enriched oxygen vacancies for efficient solar-driven water splitting. Advanced Materials, 30(20), p.1800486.

[19] Zhao, X., Feng, J., Chen, S., Huang, Y., Sum, T.C. and Chen, Z., 2017. New insight into the roles of oxygen vacancies in hematite for solar water splitting. Physical Chemistry Chemical Physics, 19(2), pp.1074-1082.

---

[20] Kashyap, R., Leal, A., Chauhan, M., Khichi, S.S., Kaur, G. and Sharma, R.K., 2023. Optimized oxygen deficient mesoporous barium doped cobalt oxide: A wonder material for green energy generation and storage. Journal of Cleaner Production, 418, p.138124.

[21] Eisazadeh, A., Kassim, K.A. and Nur, H., 2012. Solid-state NMR and FTIR studies of lime stabilized montmorillonitic and lateritic clays. Applied Clay Science, 67, pp.5-10.

[22] Aboelazm, E.A., Ali, G.A. and Chong, K.F., 2018. Cobalt oxide supercapacitor electrode recovered from spent lithium-ion battery. Chem Adv Mater, 3(4), pp.67-73.

[23] Jin, L., You, S., Ren, N. and Liu, Y., 2023. Selective activation of peroxymonosulfate to singlet oxygen by engineering oxygen vacancy defects in Ti_3CNTx MXene for effective removal of micropollutants in water. Fundamental Research, 3(5), pp.770-776.

[24] Ahn, S.H., Jin, D., Lee, C. and Lee, Y., 2023. Oxygen-Vacancy Rich $Ir_xMo_{1-x}O_y$ Nanofibers for Oxygen Evolution Reaction: pH-Universal and Electrolyte-Concentration Independent Excellent Catalytic Activity. Journal of Materials Chemistry A.

[25] Yentekakis, I.V., Goula, G., Hatzisymeon, M., Betsi-Argyropoulou, I., Botzolaki, G., Kousi, K., Kondarides, D.I., Taylor, M.J., Parlett, C.M., Osatiashtiani, A. and Kyriakou, G., 2019. Effect of support oxygen storage capacity on the catalytic performance of Rh nanoparticles for CO2 reforming of methane. Applied Catalysis B: Environmental, 243, pp.490-501.

[26] Yentekakis, I.V., Goula, G., Panagiotopoulou, P., Kampouri, S., Taylor, M.J., Kyriakou, G. and Lambert, R.M., 2016. Stabilization of catalyst particles against sintering on oxide supports with high oxygen ion lability exemplified by Ir-catalyzed decomposition of N2O. Applied Catalysis B: Environmental, 192, pp.357-364.

[27] Nikolaraki, E., Goula, G., Panagiotopoulou, P., Taylor, M.J., Kousi, K., Kyriakou, G., Kondarides, D.I., Lambert, R.M. and Yentekakis, I.V., 2021. Support induced effects on the Ir nanoparticles activity, selectivity and stability performance under CO2 reforming of methane. Nanomaterials, 11(11), p.2880.

[28] Mittal, R., Sharma, A., Bhardwaj, A.K., Bhateria, R., Bansal, S., Kashyap, R. and Bhukal, S., 2023. Removal of Chromium (VI) using Spirulina assisted Synthesized Mesoporous Iron Oxide Nanoparticles. Inorganic Chemistry Communications, p.110881.

[29] Jain, P., Shankar, S. and Thakur, O.P., 2023. Unveiling the impact of Ni_{2+}/Y_{3+} co-substitution on the structural, dielectric, and impedance properties of multiferroic spinel ferrite for hydroelectric cell application. Physical Chemistry Chemical Physics, 25(32), pp.21280-21296.

[30] Kumar, P., Sharma, R., Saifullah, M., Singh, A., Bhardwaj, V., Kansal, M.K. and Verma, V., 2023. Effect of K^+ cation doping on structural and morphology of $MgFe_2O_4$ and their role in green electrical energy generation. Journal of Alloys and Compounds, 944, p.169169.

[31] Badola, S., Shah, J., Gaur, A., Khasa, S., Rawal, D.S., Mandal, T.K., Srivastava, A.K. and Kotnala, R.K., 2023. Strategic enhancement of oxygen defects in ZnO from ZnS for water splitting to generate green electricity by hydroelectric cell. Applied Materials Today, 34, p.101904.

[32] Parray, I.A., Somvanshi, A. and Ali, S.A., 2023. Study of microstructural, ferroelectric and magnetic properties of cerium substituted magnesium ferrite and its potential application as hydroelectric cell. Ceramics International, 49(4), pp.6946-6957.

[33] Manash, A., Singh, R.K., Kumar, V., Shah, J., Das, S.B., Kumar, S.S., Kumar, N. and Kotnala, R.K., 2023. Studies on structural and magnetic properties of nanoporous Li^+ substituted $MgFe_2O_4$ nanomaterials for its application in hydroelectric cell with other areas of science & technology. Materials Today: Proceedings, 80, pp.1002-1013.